PAPER

CrossMark
←click for updates

Dipole correlation effects on the local field and the effective dielectric constant in composite dielectrics containing high-k inclusions

Elshad Allahyarov,*[abc] Hartmut Löwen[a] and Lei Zhu[c]

Mixing dielectric polymers with high permittivity (high-k) inclusions can affect their electrical properties. In actuation applications of dielectric elastomers, the polarized inclusions generate additional volume polarization-related electrostriction. In energy storage applications, it is possible to store more energy in dielectric composites because of additional polarization of the inclusions and interfaces. However, mixing an electroactive polymer with high-k inclusions also brings several disadvantages. The expulsion of the field from the interior of high-k fillers and the presence of two poles on the filler surface along the applied field direction result in higher local fields E_L near the inclusion poles. The resulting field enhancement lowers the breakdown field (E_b) threshold for the material and therefore compromises the actuation and energy storage capabilities of dielectric composites. To mitigate this issue, the dependence of E_L on the morphology of inclusion distribution, the field localization effect in chained configurations, and the role of the dipole–dipole correlation effects in the enhancement of the dipolar field of inclusions are analyzed. We show that the dipolar correlation effects are strong in large inclusion composites and their contribution to the inclusion dipole moment μ and to the local fields E_L can reach 30–50%. A new method for deriving the composite permittivity from the field E_L distribution, based on a caged probe technique, is also presented.

1 Introduction

Electroactive polymers and composites belong to the fast growing field of smart materials with promising applications in many directions.[1–15] Initially being developed for sensors and soft actuators,[16–18] vibration absorbers,[19] and damping devices,[20] these materials are now viewed as perfect building blocks for artificial muscles,[9,12,21] drug delivery systems,[22,23] nano cancer-treatment applications,[24] and other multifunctional applications.[14,25] The actuation of electroactive polymers is based on polarization processes in dielectric elastomers (DE)[1,9,21,26–30] and porous polypropylene film electrets.[10,31] Recent advances in composite DE research show that a blend of a dielectric elastomer with high-k inclusions is beneficial for the actuator properties.[26,32–47] The inclusions deliver additional volume polarization related electrostriction effects, which can either enhance the default Maxwell-stress contraction, or override the latter and turn the

composite strain into an elongation.[48–54] As shown in our recent report,[54] the electrostriction effect of the dipole–dipole interactions between polarized inclusions strongly depends on the distribution morphology of inclusions.

Besides regulating the composite actuation, the mixing of electroactive polymers with high-k inclusions seems to be beneficial for electric energy storage.[55–58] Fig. 1 schematically illustrates the advantages of filling a capacitor with a dielectric film (DF) or with a DF which is additionally impregnated with high-k inclusions. Such capacitors are the most conventional devices used in electrostatic energy storage applications. Compared to the unfilled capacitor in Fig. 1a, which can be charged up to the charge q under the applied voltage V, the DF capacitor in Fig. 1b can be charged up to the charge $q + q_m$ under the same applied voltage. Here the excess charge q_m stems from the necessity to polarize the DF layer. If the DF additionally hosts high-k inclusions as shown in Fig. 1c, one more charging term q_p, which describes the polarization effects associated with the doping particles, will contribute to the total charge on the capacitor plates. In this case, an additional demand to polarize the inclusions and the interfaces[59,60] between the inclusions and the host polymer, and to transfer a part of the external field energy to the dipole–dipole interaction energy among the inclusions makes it possible to store more energy in the composite DF.

[a] *Institut für Theoretische Physik II: Weiche Materie,*
  Heinrich-Heine Universität Düsseldorf, Universitätstrasse 1,
  40225 Düsseldorf, Germany. E-mail: elshad.allakhyarov@case.edu
[b] *Theoretical Department, Joint Institute for High Temperatures, Russian Academy*
  of Sciences (IVTAN), 13/19 Izhorskaya street, Moscow 125412, Russia
[c] *Department of Macromolecular Science and Engineering,*
  Case Western Reserve University, Cleveland, Ohio 44106-7202, USA

This journal is © the Owner Societies 2016

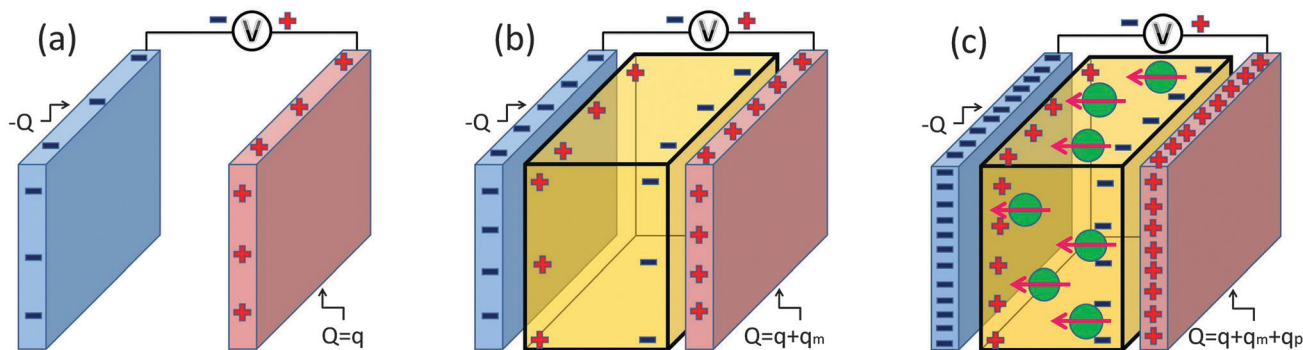*Phys. Chem. Chem. Phys.,* 2016, **18**, 19103–19117 | 19103

Fig. 1 Schematic illustration of the electrostatic energy storage in capacitors connected to a battery with a voltage V. Case (a) a capacitor without a dielectric film will be charged up to a charge q. Case (b) a capacitor with a dielectric film will be charged up to a charge $q + q_m$. Case (c) a capacitor with a dielectric film impregnated with high-k inclusions will be charged up to a charge $q + q_m + q_p$. For more details, see text.

The mixing of an electroactive polymer with high-k inclusions, however, brings several disadvantages to the functionality of composite dielectrics. For example, the expulsion of the electric field from the interior of high-k fillers and the presence of two poles on the filler surface along the applied field direction result in the formation of high local fields E_L near the inclusion surface and around its poles. These fields, especially when they overlap between neighboring inclusions, lower the breakdown field E_b threshold in the material. As a consequence, much smaller voltages can be applied to the DE composite to actuate it,[60] or store electrostatic energy in the composite DF. If the DE composite is prone to contraction under the applied field, then the overlapping of the dipolar fields of inclusions along the field direction will increase during the composite deformation. This will additionally decrease the breakdown field E_b threshold.

In order to mitigate this issue, all contributions to the spatial fluctuations of E_L from the inclusions should be carefully analyzed. First, the role of the inclusion distribution in the composite should be addressed with a focus on the field localization in chained inclusions. Second, sources of the dipole–dipole correlation effects and their role in enhancing the dipolar moment of inclusions should be elaborated. These correlation effects can become strong in large inclusion composites and consequently modify the composite electrostriction effects. In many model systems the importance of such dipole–dipole correlations is disregarded assuming that all inclusions develop the same induced dipole moment defined by their polarizability factor and the amplitude of the applied field E_0. In dilute composites with low packing fraction η for fillers the dipolar correlations are always ignored. Practically in all theoretical studies the change in the dipolar correlations and thus the revision of the dipole moments of inclusions during the composite actuation has never been addressed. Our present study shows that the contribution from the dipolar correlations to the inclusion dipole moment μ and to the local fields E_L can become significant and thus revision of the dipole moments due to dipolar correlations among inclusions should be addressed.

The purpose of the current paper is to analyze how the dipole–dipole correlation effects and the local field $E_L(r)$ distribution in dielectric composites depend on the inclusion parameters:

its packing fraction η and diameter σ_p. The issue of self-consistent stabilization of the dipoles through iteration procedures for a proper consideration of the dipole–dipole correlations is thoroughly analyzed.

The remaining part of the paper is organized as follows. In Section 2 we discuss how the mixing of dielectric polymers with polarizable fillers enhances their functional properties. In Section 3 the dielectric behavior of the composite, the dimensionality and the percolation issues are analyzed. The role of dipolar correlations in the DE composite actuation is elaborated in Section 4. Our simulation model is outlined in Section 5, where we explain the importance of the loop correction term in the calculation of the inclusion dipole moment. Simulation results are gathered and discussed in Section 6. Finally, we conclude in Section 7.

2 Enhancing the electrical properties of DE and DF composites

In practical applications, the effectiveness of the DE actuation can be measured as how much load M could be lifted by the DE actuation[29]

$$M = \frac{A}{g} Y \Sigma_M = \frac{A}{g} \varepsilon_0 \varepsilon_m \left(\frac{V}{d}\right)^2. \tag{1}$$

Here Σ_M is the Maxwell-stress strain under an open circuit condition with a constant field $E = V/d$

$$\Sigma_M = -\frac{\varepsilon_0 E^2}{Y}\left(1 - \frac{1}{\varepsilon_m}\right) \tag{2}$$

and A is the DE area across the applied field E, d is the thickness of the DE, g is the gravity acceleration constant, ε_0 is the permittivity of the vacuum, and ε_m and Y are the permittivity and the Young's modulus of the DE, respectively.

The electrostatic energy density in the elastomer under an applied field $\vec{E}$ is defined as

$$u_{DE} = \frac{1}{2\Omega}\int_{\Omega} E(\vec{r})D(\vec{r})\mathrm{d}^3\vec{r} = \frac{1}{2}\varepsilon_0 \varepsilon_m E^2 \tag{3}$$

where $D = \varepsilon_0\varepsilon_m E$ is the electric displacement, and the integration in eqn (3) is taken over the composite volume Ω. Combining eqn (1) and (3) we arrive at the following expression for the effectiveness of the DE actuation,

$$M = \frac{2A}{g}u_{DE}. \qquad (4)$$

In a similar manner, the effectiveness of energy storage in dielectric films can be evaluated as how much surface charge density

$$q = Q/A = \varepsilon_0\varepsilon_m V/d \qquad (5)$$

can be accumulated on the capacitor plates under the applied voltage V. The energy density in the dielectric film is written as

$$u_{DE} = \frac{CV^2}{2Ad} = \frac{1}{2}\varepsilon_0\varepsilon_m\left(\frac{V}{d}\right)^2 \qquad (6)$$

where C denotes the film capacitance $C = \varepsilon_0\varepsilon_m A/d$. Thus the capacitor surface charge density q from eqn (5) can be written as

$$q = \sqrt{\varepsilon_0\varepsilon_m u_{DE}}. \qquad (7)$$

From eqn (4) and (7) it is obvious that the effectiveness of the dielectric film functionality, either in actuation or in energy storage applications, explicitly depends on the energy density u_{DE} of the material. The full polarization energy of the DF or the non-actuating DE material is $U_m = u_{DE}\Omega$ under the assumption that the host polymer is nonpolar and has a homogeneous structure. For energy storage applications, the ferroelectric poly(vinylidene fluoride) (PVDF) polymer and its copolymers are potentially useful.[61–66] In this case, the energy density is modified to $u_{DE}\Omega = U_m + U_F$, where U_F accounts for the additional energy required for phase transitions, the coupling interactions among ferroelectric domains, and the domain reorientation/switching behavior. In the present study, we assume that $U_F = 0$.

When the host polymer is blended with high-k inclusions, the energy density u_c in the composite will be larger than u_{DE} in eqn (3) because of the presence of additional polarization processes. The additional polarization energy includes the polarization energy of inclusions U_p, the polarization energy of the interface area between the inclusions and the host matrix U_{pm}, and the interaction energy between the induced dipoles $U_{\mu\mu}$. Therefore, the total energy density will become

$$u_c\Omega = U_m + U_p + U_{pm} + U_{\mu\mu} \qquad (8)$$

By replacing u_{DE} in eqn (4) and (7) by u_c, we see that blending the host polymer with high-k inclusions enhances its functional properties such as lifting heavier loads in actuation or storing more charges on the capacitor plates.

During the actuation process of the DE composites, the shape dependent polarization terms U_m and $U_{\mu\mu}$ change to

$$U_m^* = U_m - \Delta U_m$$

$$U_{\mu\mu}^* = U_{\mu\mu} - \Delta U_{\mu\mu} \qquad (9)$$

where the decrease of U_m is associated with the Maxwell-stress contraction of the composite, and the decrease of $U_{\mu\mu}$ is associated with the electrostriction effect of induced dipoles. The role of the latter is elaborated in Section 6.1. In total, the released energies ΔU_m and $\Delta U_{\mu\mu}$ in eqn (9) contribute to the elastic energy of the actuation[54]

$$F_N = \Delta U_m + \Delta U_{\mu\mu} = \frac{Y\Omega}{2}(\Sigma)^2. \qquad (10)$$

Therefore, eqn (8) for the total energy of the actuated DE composite, which consists of electrostatic and elastic deformation energies, can be written as

$$u_c\Omega = U_m^* + U_p + U_{pm} + U_{\mu\mu}^* + F_N. \qquad (11)$$

Note that this expression assumes that the volume Ω and the energy density u_c do not change during the composite actuation.

3 Dielectric behavior of composites

The increase of the energy density $u_c > u_{DE}$ in dielectric composites, and thus the increase of their actuation power M in eqn (3), or their charging power q in eqn (6) implies that the host polymer permittivity ε_m in eqn (3) and (6) should be replaced by an effective permittivity ε_{eff} which is greater than ε_m. For the ε_{eff}, which is a function of two permittivities ε_p and ε_m, and the packing fraction η of inclusions, we will use the Maxwell–Garnett (MG) mixing rule[67–70]

$$\varepsilon_{eff}(MG) = \varepsilon_m\frac{2\varepsilon_m + \varepsilon_p + 2\eta\Delta\varepsilon}{2\varepsilon_m + \varepsilon_p - \eta\Delta\varepsilon} \qquad (12)$$

and the Bruggeman (BR) mixing rule[71,72]

$$\varepsilon_{eff}(BR) = \frac{1}{4}\left(\Delta\varepsilon(3\eta - 2) + \varepsilon_p + \sqrt{[\Delta\varepsilon(2 - 3\eta) - \varepsilon_p]^2 + 8\varepsilon_m\varepsilon_p}\right) \qquad (13)$$

where $\Delta\varepsilon = \varepsilon_p - \varepsilon_m$. Both the MG and BR theories are mean-field theories and do not take into account correlation and exchange effects between dipoles.[73–76] The physics underlying these mixing rules is given in Appendix A.

In general, the original BR equation can be written for any inclusion geometry in the following form[73,74]

$$\eta\frac{\varepsilon_p - \varepsilon_{eff}}{\alpha_p(\varepsilon_p - \varepsilon_{eff}) + \varepsilon_{eff}} + (1 - \eta)\frac{\varepsilon_m - \varepsilon_{eff}}{\alpha_p(\varepsilon_m - \varepsilon_{eff}) + \varepsilon_{eff}} = 0 \qquad (14)$$

where the response parameter α_p corresponds to the depolarization factor for the inclusions ($\alpha_p = 1/3$ is taken for spherical inclusions in eqn (13)) and depends on the geometry of the composite. As shown in ref. 73, eqn (14) can be used to predict the percolation threshold value for the inclusions. Assuming that the inclusions are conductive particles with $\varepsilon_p = \infty$, and then taking the limit $\varepsilon_{eff} \to \infty$, which corresponds to the percolation of the inclusions across the sample, the percolation limit is found to be $\eta_c = \alpha_p$. In other words, the depolarization factor of inclusions defines their percolation threshold using the Bruggeman approach. Usually, in experimental realizations

This journal is © the Owner Societies 2016

Phys. Chem. Chem. Phys., 2016, **18**, 19103–19117 | **19105**

of DE composites with spherical inclusions, for which $\eta_c = 0.33$, the actual packing fraction of the fillers is kept below the percolation threshold, $\eta < 0.3$ for avoiding the electrical breakdown of the material.

It should be also noted that the dimensionality of the composite is included into the BR approach through the single shape parameter α_p. Hence, only the shape of inclusions is taken into account in the BR approach, whereas the shape of the host matrix is not considered at all. On the other hand, as we have shown in our recent work,[54] the polarization of inclusions depends both on the shape of inclusions and the host matrix,

$$\vec{P}_p = \frac{\varepsilon_p - \varepsilon_m}{\varepsilon_m + (\varepsilon_p - \varepsilon_m)\alpha_p} \varepsilon_0 \varepsilon_m \left(\frac{1}{1 + (\varepsilon_m - 1)\alpha_m} \vec{E} + \sum_j \vec{E}_j \right). \quad (15)$$

Here α_m is the depolarization factor of the host matrix along the applied field E, and E_j is the electric field of other dipoles which contribute to the polarization of inclusions. In other words, the dimensionality of the composite is adequately accounted for in the framework of our simulation model.

The morphological structure of a composite material, in addition to being described by the geometry factors α_p and α_m, is often characterized by means of the a–b connectivity factor of its phases.[29] For the two-phase composites considered in this work, the term a describes the connectivity of the primary active phase, and the term b corresponds to the connectivity of the secondary passive phase. Layered composites, which are regarded as best candidates for artificial muscle applications, correspond to a 2–2 connectivity. For the DF matrix impregnated with spherical inclusions, we employ a 3–0 connectivity for the composite morphology, similar to the case considered in ref. 54.

4 The role of the $U_{\mu\mu}$ polarization term in the DE actuation

The polarization term $U_{\mu\mu}$ in eqn (8) is responsible for the electrostriction effect of dipolar interactions. The released energy $\Delta U_{\mu\mu}$ in eqn (10) generates a strain Σ_z that strongly depends on the spatial distribution $\{\vec{R}_i\}$ of inclusions.[54] In random composites $\{\vec{R}_i\}$ = rand (Ω), where the inclusions are randomly distributed in the composite volume Ω, the electrostrictive strain is negative, $\Sigma_z < 0$. Therefore, random DE composites contract stronger than the pure DE under the Maxwell-stress strain $\Sigma_M < 0$,

$$|\Sigma| = |\Sigma_z| + |\Sigma_M| > |\Sigma_M| \quad (16)$$

This behavior constitutes the main mechanism used in experimental studies to achieve higher actuation responses in high-k composites. However, for a few regular lattice composites, such as for the BCC and FCC composites, the electrostriction related effects lead to the elongation of the composite along the applied field, $\Sigma_z > 0$. Thus, the resulting strain Σ of the DE composite depends on the competition between the negative Maxwell-stress strain Σ_M and the positive electrostriction strain Σ_z,

$$\Sigma = \Sigma_M + \Sigma_z. \quad (17)$$

As it will be shown in Section 6.2, the strength of Σ_z depends on the inclusion size σ_p. Therefore, regardless of how strong Σ_M is, it is always possible to detect the right size for the dispersed inclusions in order to make $\Sigma > 0$ and elongate the composite along the applied field.

In addition to boosting the functional properties of actuators and energy storage films, the inclusions are also the source of several degrading factors to the composite operation. First, blending hard inclusions into the DE decreases its elasticity and thus compromises the composite strain Σ. Second, the expulsion of the local field E_L from the interior of inclusions, the increase of E_L near the inclusion poles, and the trapping of space charges at the inclusion–polymer interface decrease the dielectric breakdown field E_b threshold. We will use a spring-bead simulation model for the composite[54] to investigate how the local field E_L distribution and dipole–dipole correlations depend on the inclusion parameters.

5 Description of the simulation model

We consider N spherical inclusions of volume $V_p = \pi\sigma_p^3/6$ and dielectric permittivity ε_p distributed in a cubic box of size L. The packing fraction $\eta = NV_p/\Omega$ of inclusions is regulated by changing the volume Ω of the cubic box. A homogeneous distribution of inclusions is implemented in order to avoid their compact clustering and the lowering of the breakdown field E_b threshold in the material. Under the applied field $\vec{E}_0$ along the z-axis, each inclusion gains an induced dipole moment $\vec{\mu}_p^i$,[54]

$$\vec{\mu}_p^i = \vec{\mu}_p^0(E_0) + \vec{\mu}_p(E_j) \quad (18)$$

where the first part $\vec{\mu}_p^0$ is the pure dipole moment of a spherical inclusion i,

$$\vec{\mu}_p^0 = 4\pi\varepsilon_0 \left(\frac{\sigma_p}{2}\right)^3 \frac{\varepsilon_p - \varepsilon_m}{\varepsilon_p + 2\varepsilon_m} \vec{E}_0 \quad (19)$$

and the second part $\vec{\mu}_p(E_j)$ is the excess dipole moment of the inclusion i from the fields of other inclusions j ($1 \leq j \leq N$, $j \neq i$) and their periodic images in neighboring cells,

$$\vec{\mu}_p\left(\vec{E}_j\right) = 4\pi\varepsilon_0 \left(\frac{\sigma_p}{2}\right)^3 \frac{\varepsilon_p - \varepsilon_m}{\varepsilon_p + 2\varepsilon_m} \sum_j^N \varepsilon_m \vec{E}_j\left(\vec{\mu}_p^j\right) \quad (20)$$

The field $\vec{E}_j$ in eqn (20) depends on the dipole moment $\vec{\mu}_p^j$ of inclusion j, thus the dipole moment of each inclusion depends on the dipole moment of all other inclusions. In other words, eqn (18)–(20) should be solved through consecutive iterations for stabilizing the dipole moments $\vec{\mu}_p^i$ of inclusions. The importance of such dipolar correlation effects has been overlooked in most theoretical studies assuming that they are negligible in dilute (i.e. small η) composites.

For the direct evaluation of the dipolar correlation effects in eqn (18)–(20) we introduce a loop correction term $\langle\mu\rangle_L$ to the

19106 | *Phys. Chem. Chem. Phys.*, 2016, **18**, 19103–19117

This journal is © the Owner Societies 2016

pristine dipole moment μ_p^0 of inclusions, which we define as

$$\langle \mu \rangle_L = \frac{1}{N} \frac{\sum_i^N \mu_p^i}{\mu_p^0} - 1. \tag{21}$$

Here all inclusion dipoles μ_p^i are stabilized by solving eqn (18)–(20) by iterative loops, and the loop correction is averaged over them. Without the dipole stabilization procedure, the loop correction term is $\langle \mu \rangle_L = 0$. The $\langle \mu \rangle_L$ explicitly contains the contribution from the fields of all other inclusions, and implicitly includes the dipole–dipole correlation effects between the inclusions. As it will be shown below, these loop corrections can cause twice stronger local fields in the composite compared to the case when no loop corrections are included.

Once all the dipoles $\vec{\mu}_p^i$ in the composite are stabilized, the system is then ready for running MD simulations to calculate the composite strain Σ_z and the local field distribution E_L. We use $N\Omega T$ ensemble molecular dynamics simulations using a Verlet algorithm and a Nose thermostat for the inclusions in the host polymer. Elastic properties of the host matrix are modeled through springs with spring constants χ which connect each inclusion to its n_b nearest neighbors. We identify the correct χ for which the simulation predicted the Young's modulus

$$Y_{MD} = \frac{3\chi}{\Omega} \frac{\sum_i^{x,y,z} \Delta r_{ij}^2}{\sum_i^{x,y,z} \Sigma_i^2 + 2\Sigma_i} \tag{22}$$

to be equal to the composite modulus Y. In eqn (22) $\Delta r_{ij} = |\vec{r}_{ij} - \vec{r}_{ij}^0|$ is the bond length deformation between the inclusions i and j, and Σ_i is the strain along the $i = x, y, z$ axis. For the random composite we chose $n_b = 14$ from the list of the first nearest neighbors for each inclusion. The nearest-neighbor separation distance in the random inclusion distribution is defined as $r_p = 0.554(V_p/\eta)^{1/3}$.[77] In the BCC composite, where the inclusions occupy the nodes of the BCC lattice, each inclusion is connected to its 8 neighbors from the first coordination shell of radius $r_p\sqrt{3}/2$, and 6 neighbors from the second coordination shell of radius r_p, thus making the total $n_b = 14$ again. The lattice constant of the BCC structure is defined as $r_p = (2V_p/\eta)^{1/3}$.

In simulation runs the evolution of the stress-free initial system with $E = 0$ to a new state with balanced electrostatic and elastic forces is controlled by the equivalence of the pressure components in all three directions. The pressure is calculated using the force virials

$$P = \frac{1}{3\Omega} \sum_{j>i}^N \vec{r}_{ji} \cdot \vec{\Xi}_{ji} \tag{23}$$

where the forces $\vec{\Xi}_{ij}$ between the inclusions i and j include both the electrostatic forces $\vec{F}_{ji}$ between the dipoles i and j, and the elastic forces

$$\vec{F}_{ji}^{elastic} = \chi(r_p - r_{ji})\frac{\vec{r}_{ji}}{r_{ji}}. \tag{24}$$

Here $\vec{r}_{ji} = \vec{r}_i - \vec{r}_j$, and for the elastic forces the summation in eqn (23) goes over the n_b neighbors of the inclusion i.

The long-range nature of dipole–dipole interactions in $\vec{F}_{ji}$ is handled using the Ewald's summation technique.[78–80] For the full description of the simulation model the reader is referred to ref. 54.

For the calculation of the local field $E_L(\vec{r})$ distribution we create a temporary mesh network $\{\vec{\ell}_i\} = \{x_i, y_i, z_i\}$ in the composite with 400 points in each direction. The components of $E_L(\vec{\ell}_i)$ are calculated as a sum of the dipolar fields $\vec{E}_j$ of all inclusions and their periodic images in neighboring cells,

$$E_L(x_i) = \sum_j^N E_j(x_i), \quad E_L(y_i) = \sum_j^N E_j(y_i),$$
$$E_L(z_i) = \sum_j^N E_j(z_i) + E_0 \tag{25}$$

where x_i, y_i, and z_i are the coordinates of mesh points $\vec{\ell}_i$. The amplitude of the total field at the mesh points $\vec{\ell}_i$ is defined as

$$E_L(\ell_i) = |\vec{E}_L(\ell_i)| = \sqrt{E_L^2(x_i) + E_L^2(y_i) + E_L^2(z_i)} \tag{26}$$

6 Results

6.1 Dipole–dipole correlation effects in composites

The loop correction $\langle \mu \rangle_L$ is plotted in Fig. 2 as a function of η in the polarized composite prior to its actuation. For the BCC composite $\langle \mu \rangle_L = 0$ because of the mutual cancellation of the field contributions from the neighboring dipoles. In random composites $\langle \mu \rangle_L$ has quadratic η dependence. At $\eta = 0.3$ the contribution from $\langle \mu \rangle_L$ reaches about 40% of the value of μ_0. As a result, the actuation of the DE will be much stronger compared to its actuation with dipoles μ_p^0. It is also obvious that during the DE actuation the loop corrections should always
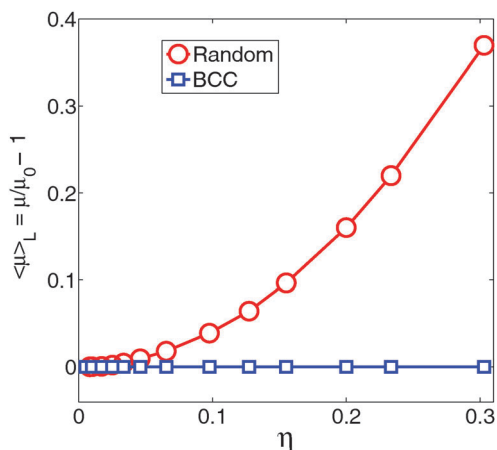

Fig. 2 Loop correction term $\langle \mu \rangle_L$ from eqn (21) for the dipole moment of inclusions as a function of inclusion packing fraction η before the composite actuation. Line with circles – random composite and line with squares – regular BCC composite. The other system parameters are: applied field $E_0 = 50$ MV m^{-1}, $\varepsilon_m = 2$, $\varepsilon_p = 100$, $\sigma_p = 2$ μm, and $Y = 0.1$ MPa.

This journal is © the Owner Societies 2016

Phys. Chem. Chem. Phys., 2016, **18**, 19103–19117 | **19107**

be maintained in order to guarantee that the change in the inclusion distribution morphology following the shape change of the composite happens under the condition of fully stabilized dipoles. While in experimental studies the adjustment of dipoles to the shape change of the sample is instant and self-consisting, in numerical approaches this adjustment is usually implemented through the iterative loops. Our simulations show that the number of loop correction steps for stabilizing the dipoles μ_p^i in eqn (18)–(20) depends on η, and for high $\eta > 0.2$, it reaches several hundred iteration steps. In computer simulations the dipole moment stabilization process can be tracked and the dipolar correlation effects can be separately examined. Note that in experimental studies, such stabilization process happens instantly and the loop correction term cannot be estimated separately.

6.2 Evolution of the dipole–dipole correlations during the composite deformation

Simulation results of the composite strain are plotted in Fig. 3 for the random and BCC composites as a function of the inclusion diameter σ_p. The field $E_0 = 50$ MV m^{-1} was applied along the z axis, and the host matrix and inclusion permittivities were $\varepsilon_m = 2$ and $\varepsilon_p = 100$, respectively, and the packing fraction was fixed to $\eta = 0.0083$. For the elasticity modulus of the host matrix we choose $Y = 0.1$ MPa which is a typical value for dielectric elastomers. The inclusion diameter is varied between 200 nm and 4 μm. A similar composite with $\sigma_p = 200$ nm and $\eta = 0.0083$ was considered in our previous paper[54] where the following strain values were reported: $\Sigma_z = -5\%$ for the random composite, $\Sigma_z = +2\%$ for the BCC composite, and $\Sigma_M = -11\%$ for the Maxwell-stress strain. Our simulation results in Fig. 3 clearly indicate that as σ_p increases, or equivalently, as the induced dipole moment μ_0 increases, the strength of the electrostriction driven strain Σ_z also increases. For the random composite the electrostriction driven negative strain Σ_z becomes twice stronger than Σ_M for $\sigma_p > 2$ μm. Thus, making the inclusions bigger at a fixed η is beneficial for obtaining stronger composite actuation. For $\sigma_p > 2.3$ μm the positive electrostriction strain in the BCC composite overrides the Maxwell-stress strain Σ_M. As a result of this, the total strain Σ of the composite becomes a net elongation deformation along the field direction.

According to eqn (11), the composite actuation Σ_z can be viewed as an attempt of the composite to minimize its electrostatic energy through a shape change. Such minimization is followed by the strengthening of dipole–dipole correlation effects, which obviously affects the loop correction $\langle \mu \rangle_L$ term in eqn (21). This correction term is plotted in Fig. 4 as a function of σ_p for the strain data Σ_z shown in Fig. 3. It is seen that in an actuated composite with non-zero Σ_z the loop correction $\langle \mu \rangle_L$ becomes stronger. For example, as seen from Fig. 2, in a non-actuated composite the loop correction is nearly negligible for the random composite with $\sigma_p = 2$ μm and $\eta = 0.0083$. Now, when the composite is actuated, the loop correction reaches almost 15% at the same σ_p and η. Qualitatively a similar increase of $\langle \mu \rangle_L$ is visible for the BCC composite in Fig. 3. It is worth noting that the loop correction is always positive regardless of the sign of the strain Σ_z. In other words,
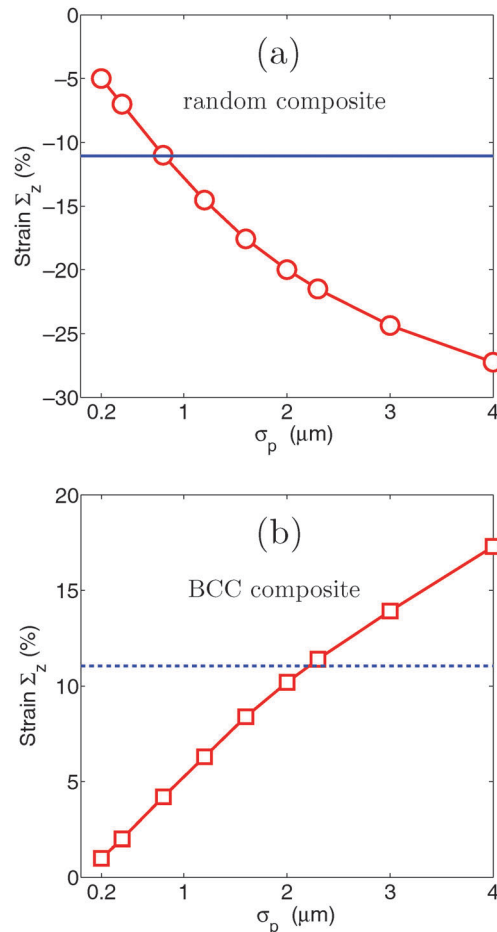

Fig. 3 Dependence of the DE composite strain Σ_z on the inclusion size. (a) Random composite and (b) regular BCC composite. The Maxwell-stress strain Σ_M is shown as a horizontal blue line in (a), and its modulus is shown as a dashed blue line in (b). The other system parameters are: $\eta = 0.0083$, $E_0 = 50$ MV m^{-1}, $\varepsilon_m = 2$, $\varepsilon_p = 100$, and $Y = 0.1$ MPa.
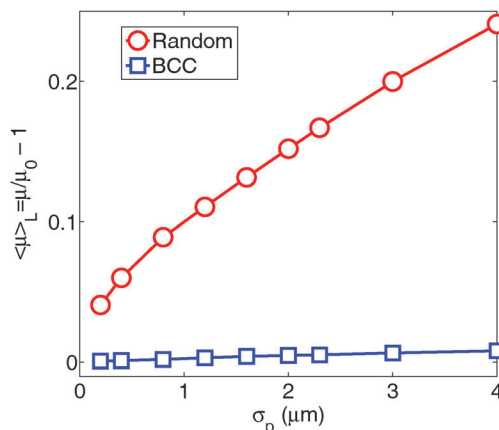

Fig. 4 Loop correction term $\langle \mu \rangle_L$ from eqn (21) for the dipole moment of inclusions as a function of the inclusion size σ_p for the actuated DE composite. Line with circles – random composite and line with squares – regular BCC composite. The other system parameters are: applied field $E_0 = 50$ MV m^{-1}, $\varepsilon_m = 2$, $\varepsilon_p = 100$, and $Y = 0.1$ MPa.

during the composite actuation the dipoles displace in a such way that their dipole moments get an additional enhancement. This is possible only when the parallel oriented dipoles tend to form nose-to-tail conformations. Or, the actuation of the composite lowers its electrostatic energy by increasing the dipole–dipole attraction between the induced dipoles.

The interesting question is why larger inclusions at a fixed η stimulate stronger strains and loop corrections. If σ_p increases α times, $\sigma_p^{(2)} = \alpha\sigma_p^{(1)}$, then the nearest-neighbor distance $r_p^{(2)} = 0.5 \eta^{-1/3}\sigma_p^{(2)} = \alpha r_1^{(2)}$ between the inclusions will increase α times, and the dipole moment of the inclusion $\mu_0^{(2)} = \alpha^3\mu_0^{(1)}$ will increase α^3 times. Therefore, for a pair of inclusions with dipoles $\mu_0^{(2)}$ separated by a distance $r_p^{(2)}$, the field E_2 created by one of the inclusions at the center of the other inclusion is

$$E_2 = \frac{1}{4\pi\varepsilon_0\varepsilon_m}\frac{\mu_0^{(2)}}{\left(r_p^{(2)}\right)^3} = \frac{1}{4\pi\varepsilon_0\varepsilon_m}\frac{\alpha^3\mu_0^{(1)}}{\alpha^3\left(r_p^{(1)}\right)^3} = E_1 \qquad (27)$$

In other words, the field distribution in the composite should not change when σ_p is increased at a fixed η. However, this conclusion contradicts the results shown in Fig. 2. A possible reason for the increase of $\langle\mu\rangle_L$ in larger inclusion composites might be the increase of the coupling constant $\Gamma = V(\mu_i,\mu_j)/k_BT$, which determines the strength of the interaction energy $V(\mu_i,\mu_j)$ between the dipoles μ_i and μ_j with respect to their thermal energy k_BT. By testing the strength of the interaction potential $V_k = \mu_0^{(k)}E_k$ between the dipoles ($k = 1$ for composites with smaller inclusions of size σ_1, and $k = 2$ for composites with larger inclusions of size $\sigma_2 = \alpha\sigma_1$),

$$V_2 = \mu_0^{(2)}E_2 = \frac{1}{4\pi\varepsilon_0\varepsilon_m}\frac{\left(\mu_0^{(2)}\right)^2}{\left(r_p^{(2)}\right)^3} = \frac{1}{4\pi\varepsilon_0\varepsilon_m}\frac{\alpha^6\left(\mu_0^{(1)}\right)^2}{\alpha^3\left(r_p^{(1)}\right)^3} = \alpha^3 V_1 \quad (28)$$

we see that indeed the dipole–dipole interaction potential in a larger inclusion composite increases α^3 times. Therefore, the reason for stronger loop corrections in larger inclusion composites is the increased coupling constant Γ between neighboring inclusions.

6.3 Local field E_L distribution in the composite

The enhancement of the loop corrections in Fig. 2 and 4 directly indicates that the volume averaged local field

$$E_L = \frac{1}{\Omega}\int_\Omega E_L(\vec{r})d^3r \qquad (29)$$

is also enhanced across the composite. However, it should be noted that this enhancement is a volume averaged effect, and in some areas of the composite an opposite effect, *i.e.*, the field depletion effect, might occur. First, the local field $E_L(\vec{r})$ is strongly inhomogeneous in the composite.[5,44,55,81–83] The field is high at two poles of the inclusion and between two inclusions oriented along the applied field (vertical direction), whereas it is weak between horizontally placed inclusions. When the packing fraction η increases, according to our recent results in ref. 55, the inhomogeneity of $E_L(\vec{r})$ distribution becomes more sharper. Second, for some particular inclusion configurations
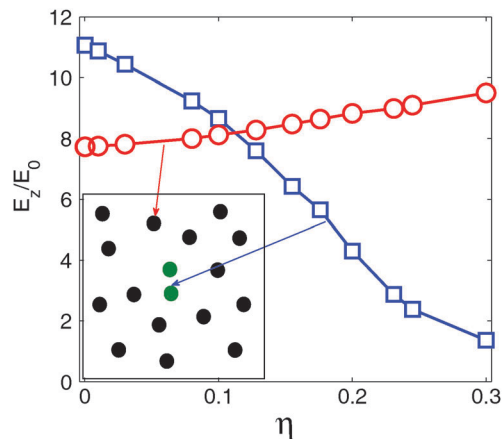

Fig. 5 The dependence of the local field E_z at the poles of inclusions on the packing fraction η. A pair of inclusions are fixed at a separation distance $\Delta_z = 1.5\sigma_p$ along the z-axis, as shown in the inset picture. Blue line – the value of E_z at the inner pole of the pair. Red line – the value of E_z at the north pole of bulk inclusions. The other system parameters are: applied field $E_0 = 50$ MV m^{-1}, $\sigma_p = 70$ nm, $\varepsilon_p = 120$, $\varepsilon_m = 2.25$.

the field enhancement concept can completely fail. For example, we consider a pair of inclusions placed along the z-axis with a fixed separation distance $\Delta_z = 1.5\sigma_p$. We gradually increase the packing fraction η by decreasing the system volume Ω while keeping the pair fixed. Simulation results for $E_L(\vec{r})$ at the inclusion poles show that the field at the inner pole area of the pair decreases as η increases, see the blue line in Fig. 5. In contrast, the field enhancement effect at the poles of isolated and individual inclusions is positive, see the red line in Fig. 5. This specific example clearly illustrates that while the volume averaged E_L always shows an enhancement as η increases, the local field distribution $E_L(\vec{r})$ might get a depletion effect within some specific inclusion distribution in the composite (*e.g.*, a cluster of particles).

For the random and BCC composites we plot a 3D $E_L(\ell_i)$ distribution in Fig. 6. In Fig. 6A and C the total field $E_L(\ell_i)$ from eqn (26) with and without loop corrections $\langle\mu\rangle_L$ for the random composite are shown. A detailed analysis of these figures reveals that the loop corrections are mostly localized in areas of chained clusters in Fig. 6C. In these areas the loop corrections make $E_L(\vec{r})$ twice stronger compared to the case of no loop correction in Fig. 6A. In some areas of the chained configuration in Fig. 6C the field E_L reaches 18 E_0 (about 1 GV m^{-1}), which is twice larger than the typical breakdown field for dielectric elastomers $E_b \approx 500$ MV m^{-1}. Therefore, in the experimental realization of such random composites, specific care should be taken to avoid any accidental chain-like clustering of inclusions along the applied field. Otherwise, the composite is prone to electrical breakdown.

In Fig. 6B and D the z-components of the field distribution $E_z = E_L(z_i)$ are shown with the purpose of highlighting the occurrence of negative field patches around the inclusions. These patches with $E_z \approx -E_0$ are oriented perpendicular to the applied field direction. The formation of negative field patches is a consequence of huge field localization between chained

This journal is © the Owner Societies 2016

Phys. Chem. Chem. Phys., 2016, **18**, 19103–19117 | **19109**
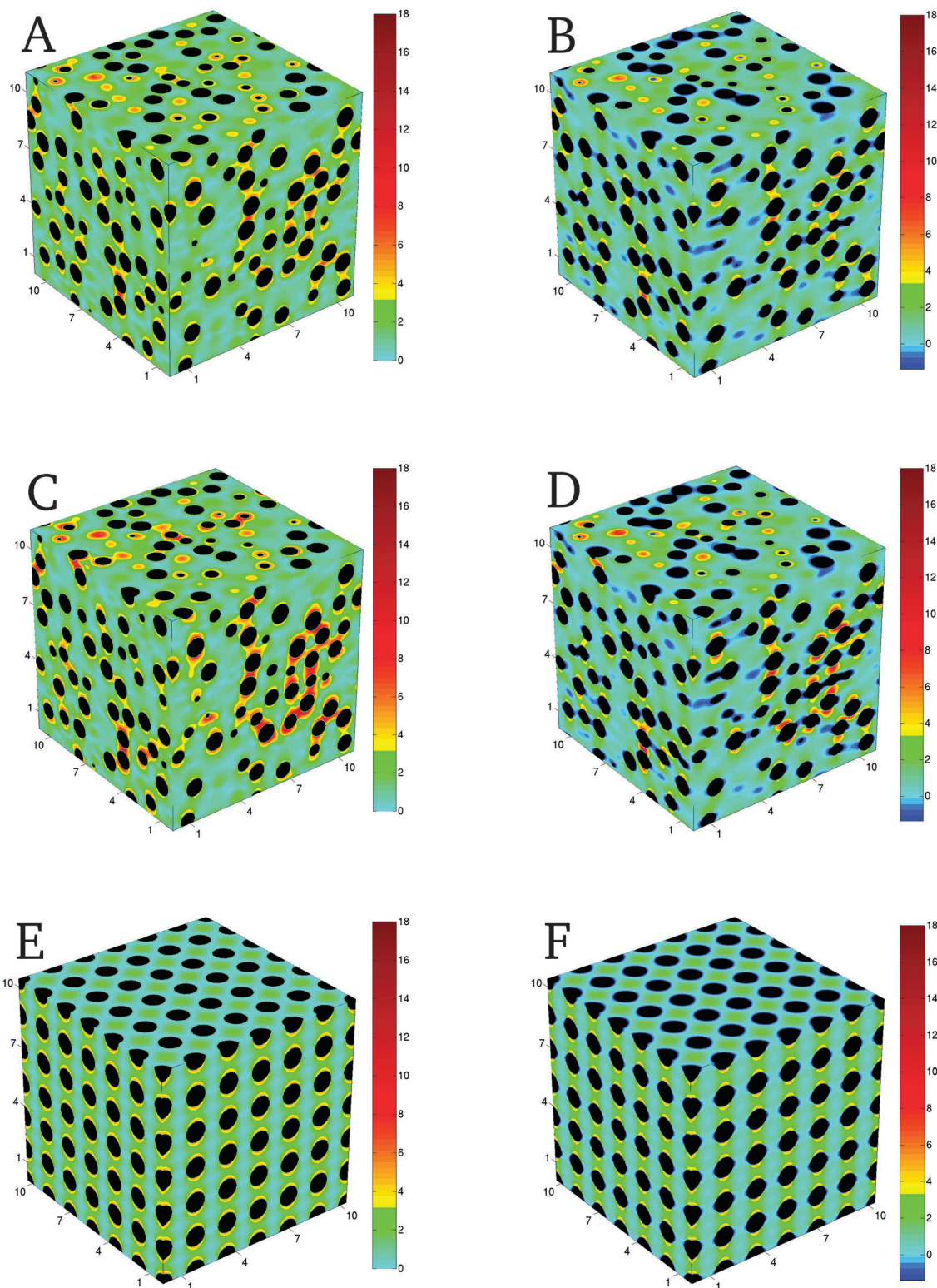
Fig. 6   3D distribution of the local fields $E_L(\vec{r})/E_0$ and $E_z(\vec{r})/E_0$ in the DF composites with $\eta = 0.2$. (A–D) Are for the random composite, (E and F) are for the BCC composite. (A) The initial field distribution $E_L(\vec{r})/E_0$ without loop corrections, (B) the initial field distribution $E_z(\vec{r})/E_0$ without loop corrections, (C) the final field distribution $E_L(\vec{r})/E_0$ with loop corrections, (D) the final field distribution $E_z(\vec{r})/E_0$ with loop corrections, (E) the final field distribution $E_L(\vec{r})/E_0$ with loop corrections, and (F) the final field distribution $E_z(\vec{r})/E_0$ with loop corrections. The other system parameters are: $E_0 = 50$ MV m^{-1}, $\varepsilon_m = 3$, $\sigma_p = 100$ nm, $\varepsilon_p = 1000$.

inclusions. In other words, if the patches occupy more area in the composite, then the higher field will localize in chained clusters, and the composite will contract. The high field domains $5 < E_z/E_0 < 13$ are separately shown in Fig. 7. The composite will
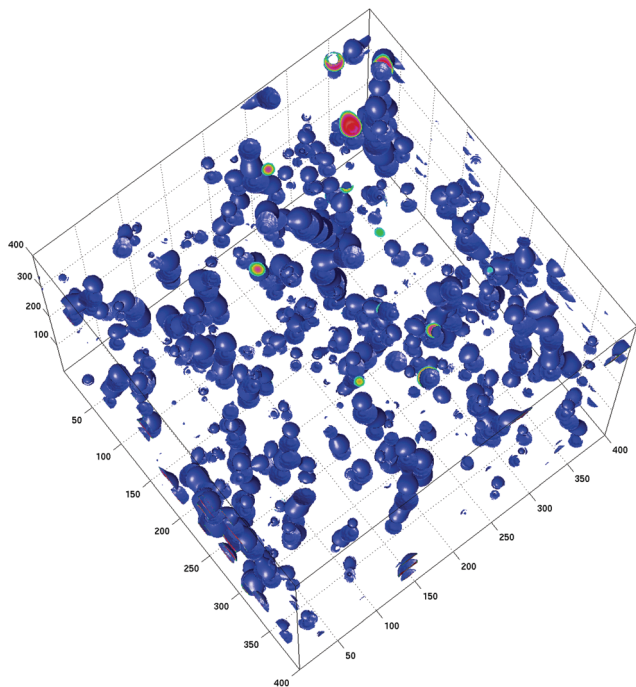
Fig. 7 Detailed local field distribution in the range $5 < E_z/E_0 < 13$ from Fig. 6D.

primarily shrink along the string-like field domains. At the same time, these string-like areas of the composite will be more vulnerable to the dielectric breakdown.

In Fig. 6E and F, as a comparison to the random composite case, we plot the $E_L(\ell_i)$ and E_z distributions in the regular BCC composite. Here the field fluctuations along and perpendicular to the applied field are moderate, $E_L(\vec{r})$ reached $4E_0$ at the inclusion poles, and $-E_0$ at the inclusion equator. Neither field localization nor negative field patches are detected. The regular BCC composite elongates only within some window of the initial distortion ratio parameter $\theta = c/a$,[54] where c is the lattice constant of the regular lattice in the z axis direction, and a is the lattice constant in the x and y directions. Therefore, it will be interesting to compare the field distributions in contracting and elongating BCC composites in order to understand the link between the morphology of $E_L(\ell_i)$ or E_z and the strain Σ_z. This task is beyond the scope of the present research.

6.4 Calculation of the composite permittivity from the distribution of $E_L(\vec{r})$

In experimental studies and engineering applications, the effective permittivity ε_{eff} of the composite is usually determined using broadband dielectric spectroscopy,[55] finite element method (FEM) based approaches,[44,81,82] the finite-difference time-domain (FDTD) method,[84] and an equivalent capacitance model.[85] In the simulations the effective permittivity ε_{eff} can be determined from

$$\langle \varepsilon(r)E^2(r) \rangle_\Omega = \varepsilon_{eff} \langle E(r) \rangle_\Omega^2 \qquad (30)$$

in which $E(r)$ is the local electric field at position r in the composite, $\varepsilon(r)$ is the local dielectric constant, and angular

brackets denote the volume average.[86] For our two-phase composite model, $\varepsilon(r) = \varepsilon_p$ inside the particles, and $\varepsilon(r) = \varepsilon_m$ in the host matrix. A direct implementation of eqn (30) is only possible when the local field $E(r)$ is roughly homogeneous across the dielectric elastomer, which is the case of low dielectric contrast composites with $\varepsilon_p/\varepsilon_m < 10$.[87] Otherwise, for high-k inclusion composites with high dielectric contrast, huge field gradients near the poles and between the inclusions limit the proper averaging of $E(r)$ and $E^2(r)$ in eqn (30).[88] In this case specific care should be taken for accurately solving Maxwell equations near the singular points of polarized inclusions. Nevertheless, and rigorously speaking, while it is possible to determine the local field at any given point in the composite, it is not possible to determine it at all composite points for the proper volume averaging in eqn (30).

The field averaging procedure can be sufficiently simplified for a high dielectric contrast, $\varepsilon_p/\varepsilon_m > 30$, composites with no clustering condition for inclusions. The left part of eqn (30) can be rewritten as

$$\langle \varepsilon(r)E^2(r) \rangle_\Omega = \langle \varepsilon_p E_p^2 \rangle_\Omega + \langle \varepsilon_m E_L^2 \rangle_\Omega \qquad (31)$$

where E_p is the local field inside the inclusion,

$$E_p = \frac{3\varepsilon_m}{\varepsilon_p + 2\varepsilon_m}(E_0 + \eta E_0). \qquad (32)$$

Here we include the additional field term ηE_0, which corresponds to the total local field created by other inclusions j at the center of the inclusion i. For the E_L in the host matrix we assume $E_L = \gamma E_0$, with the enhancement factor $\gamma > 2$. In composites with homogeneous distribution of inclusions, each inclusion can be assumed as an individual particle sitting in a spherical shell of the host matrix of volume V_1. Then, by partitioning the whole system into N spherical volumes V_p and N shell volumes V_{sh}, $\Omega = NV_p + NV_{sh}$, or $NV_{sh}/\Omega = 1 - \eta$, for eqn (31), we get

$$\langle \varepsilon(r)E^2(r) \rangle_\Omega = \frac{9\varepsilon_p \varepsilon_m^2}{(\varepsilon_p + 2\varepsilon_m)^2}\eta(1 + \eta)^2 E_0^2 + \gamma^2 \varepsilon_m E_0^2 (1 - \eta). \qquad (33)$$

The ratio of the second term to the first term on the left side of this equation

$$\Theta_1 = \gamma^2 \frac{\varepsilon_p}{9\varepsilon_m}\left(1 + 4\frac{\varepsilon_m}{\varepsilon_p} - \left(\frac{\varepsilon_m}{\varepsilon_p}\right)^2\right)\frac{1 - \eta}{\eta(1 + \eta)^2} \qquad (34)$$

is a suitable measure of the relative contribution of the particle interiors to the effective permittivity ε_{eff}. For typical high-k inclusion composites with $\varepsilon_p/\varepsilon_m > 30$, $\gamma > 2$, and $\eta < 0.3$, for the lower bond of Θ_1, we get $\Theta_1 > 20$. This means that the contribution from the energy density inside the inclusions to ε_{eff} is less than 5% from the contribution of the field energy in the host matrix. Similar arguments can be used to estimate the field average $\langle E(r) \rangle$ in right side averaging in eqn (30). Here, for a similar parameter Θ_2

$$\Theta_2 = \gamma \frac{1 - \eta}{\eta(1 + \eta)}\frac{\frac{\varepsilon_p}{\varepsilon_m} + 2}{3} \qquad (35)$$

which measures the relative contribution of the particle interiors to ε_{eff}, and for the same composite parameters $\varepsilon_p/\varepsilon_m > 30$, $\gamma > 2$,

and $\eta < 0.3$, we get $\Theta_2 > 40$. Thus, the field averaging in high-k composites has no more than 3% contribution from the particle interiors. Therefore, based on the theoretical predictions for the parameters Θ_1 and Θ_2, up to the packing fractions $\eta < 0.3$ it is completely safe to use only the host matrix averaging in eqn (30) for high-k composites.

For the calculation of $\langle E_L \rangle_\Omega$ and $\langle E_L{}^2 \rangle_\Omega$ in the host matrix, we create a field-testing probe of octahedral shape with six inclusions occupying its nodes, and another probe particle is placed at its center as shown in Fig. 8. The cage nodes have the same properties as the inclusions: they develop induced dipole μ_p^i under the applied field E_0 and react to the polarization field of other inclusions. The probing cage is then placed at the positions $\vec{r}_c$ in the composite, and the average of the local field $E_L(r_c)$ at its center is calculated as,

$$\langle E_L(\vec{r}_c) \rangle = \left\langle \sum_{j=1}^{N-7} \vec{E}_j\left(\mu_p^i\right) \right\rangle_\Omega . \quad (36)$$

Here the averaging $\langle \cdots \rangle_\Omega$ is done by random insertions of the cage into the vacant positions in the composite. The role of the octahedral cage is twofold. First, the cage nodes shield the probe particle from the close proximity of other inclusions and therefore minimizes the effect of huge field fluctuations at the cage center $\vec{r}_c$. Second, for the chosen geometry of the cage, the combined effect of the cage node dipoles at the probe center is zero, i.e., the probe particle exclusively reacts only to the field of other composite inclusions.

For high packing fractions $\eta > 0.1$ the volume averaging in eqn (36) has bad statistics because of the decreasing number of successful probe insertions into the composite. For these cases it is more efficient to place the probing cage at the center of the simulation box $\vec{r}_c = 0$, and then generate random inclusion
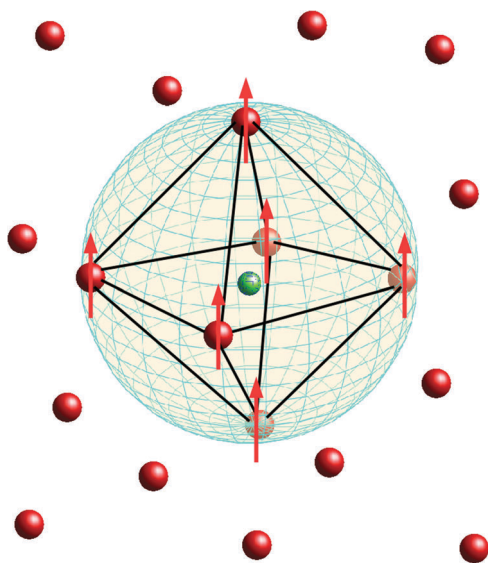

Fig. 8 Schematic illustration of the octahedral cage devised to probe the local field in the composite. The central particle shown in green is the probe particle at the center of which the field $E_L(\vec{r})$ is measured. Only the dipoles of the cage-forming inclusions are shown.
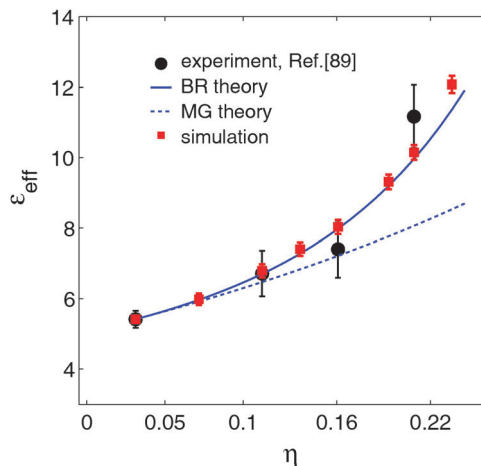

Fig. 9 Dependence of $\varepsilon_{eff} = \langle \varepsilon(r) E^2(r) \rangle_\Omega / \langle E(r) \rangle_\Omega{}^2$ on the inclusion packing fraction η in the random composite. A direct calculation of ε_{eff} using the full $E(r)$ in the simulation box and the calculation based on a probe cage placed in the host matrix produce similar results. Squares – our simulation result, dashed line – the MG fitting, full line – the BR fitting, and circles – the experimental results of ref. 89. The other system parameters are: $E_0 = 100$ MV m^{-1}, $\varepsilon_m = 4.3$, $\sigma_p = 50$ nm, $\varepsilon_p = 150$.

distributions around the cage. Repeating this procedure several hundred times with different random particle generations guarantees good statistical averaging in eqn (36).

Calculated ε_{eff} from eqn (30) is plotted in Fig. 9 as a function of η for $E_0 = 100$ MV m^{-1}, $\varepsilon_m = 4.3$, $\varepsilon_p = 150$, and $\sigma_p = 50$ nm, which correspond to the experimental parameters used in ref. 89. These specific experimental data were chosen because of the fact that, unlike other experimental studies, in ref. 89, a high-dielectric contrast and a matrix-free composite was directly grown from hairy nanoparticles. This procedure guarantees a homogeneous distribution of inclusions, a necessary condition for the direct comparison between experimental and simulation results. Additionally, the surface-initiated polymerization from the nanoparticles in ref. 89 also makes it possible to employ a bare-core model for the inclusions (used in the current work) for the experimental results. A similar composite growth procedure from hairy nanoparticles was also implemented in a recent experimental study.[5] In this case, however, the nanoparticles had a low dielectric permittivity $\varepsilon_p = 4$, which practically had little contribution to the effective permittivity of the composite. On the other hand, if experimental studies show cluster formation in the matrix, computer simulations should be adequately modified to generate similar clusters with the corresponding input parameters for their size and the average distance between them.

For $\eta = 0.22$ in Fig. 9, the highest packing fraction used in ref. 89, $\Theta_1 = 38$ and $\Theta_2 = 36$. This means that the contribution from the interior of inclusions to ε_{eff} is less than 3% compared to the total contribution from the whole composite volume. As it is expected, ε_{eff} shown in Fig. 9 increases with the packing fraction of inclusions. The MG and BR mixing rules given by eqn (12) and (13) respectively, are also shown for the comparison. The MG result underestimates the calculated effective permittivity, whereas the BR result is in good agreement with simulated ε_{eff}.

A small deviation between the BR mixing rule and our simulation results at higher $\eta > 0.22$ might be a consequence of the loop correction term given by eqn (21), which is not accounted for in the mixing rule approaches. There is also a small discrepancy between our findings and the experimental results of ref. 89. We did additional simulations with an increased particle size $\sigma_p = 70$ nm, and got the same data for ε_{eff}. In other words, a moderate change in the particle size, while keeping the packing fraction the same, has very small impact on ε_{eff}. Obviously, at high η the dipolar approach should be replaced with more realistic representations of the particle polarization. The implementation of two opposite charges on the particle poles might be a good starting approximation for taking into account higher order multipole contributions to the inclusion–inclusion interactions.

As shown in ref. 73 and 74 the polymer–particle bounding layer starts to play an essential role in nanometer particle sizes. Consequently, the Bruggeman approach should be modified by assuming a core–shell particle in a host matrix and by adding an additional term to eqn (14). In this case ε_{eff} also becomes a function of the particle size σ_p because the shell fraction depends on σ_p. Assuming a typical shell thickness of a few (2–5) nanometers, it is believed that for the particles bigger than 100 nm the bare-core model should be a reliable approximation. As has been mentioned above, for the surface-initiated polymerization from the nanoparticles, the bare-core approach is always an applicable model regardless of the size of the inclusions.

7 Conclusions

The mixing of dielectric elastomers or films with high-k inclusions enhances their functional properties such as the strength of their actuation and their energy storage capabilities. Such enhancement is linked to the additional volume polarization related electrostriction effects enabled by the inclusions. The polarization of inclusions and electrostriction effects can be described at three different levels. Within the first and the lowest level, it is assumed that the polarization of the inclusion only depends on the applied field and there is no field exchange between the dipoles which can alter the amplitude of dipoles. Such an approach is applicable to dilute composites with low packing fraction for inclusions, and is often used in the actuation of ferrogels. Within the second level, the amplitude of the induced dipoles, in addition to the applied field, also reacts to the field of other dipoles. However, this field exchange contribution is assumed to not depend on the spatial distribution of inclusions. Finally, in the third and the most realistic level, the field exchange and correlation effects between dipoles are fully taken into account. The current study is based on this third level of approximation for the electroactive composites. We have shown that the dipole moments of inclusions should be carefully stabilized through iterative loops in order to properly account for the dipole–dipole correlation and field exchange effects. According to our simulation results, the loop correction term strongly depends on the inclusion parameters, and might substantially alter the local field distribution in the composite,

along with boosting the electrostriction effects in the composite. Because of the positive feedback from the loop corrections to the inclusion dipole moment, the coupling between dipoles increases which leads to higher composite strains. At the same time positive loop corrections point to the increasing of the dipole–dipole attraction during the composite actuation. A detailed analysis of the 3D local field distribution in the composite reveals that the loop corrections are mostly localized into the areas of chained clusters, where the field becomes twice stronger compared to the field distribution with no loop corrections. However, these areas of localized field in the composite are responsible for the lowering of the breakdown field E_b threshold, which compromises the actuation and energy storage capabilities of dielectric composites.

A new method for deriving effective permittivity of the composite from the calculated local field distribution is presented. It is shown that in high-k composites the contribution from the particle interiors to the ε_{eff} is negligible. For the proper averaging of the local field E_L in the host matrix we devise a shielding cage with a field-probing particle in its center. The calculated ε_{eff} as the ratio of the averaged field energy to the energy of the averaged field appears in good agreement with empirical mixing rules.

The implications of presented results are important for devising new and reliable electroactive composites. First, for keeping the breakdown field E_b high, according to our results, a proper optimization of the size, permittivity, packing fraction, and distribution of inclusions should be carried out. A detailed knowledge on the field enhancement effect, which also implies a proper accounting for the dipolar correlation effects, is the necessary tool for preventing the breakdown of the DE and DF composites in the fast growing field of artificial muscles, robotic and mechatronic applications.[3,9,90] Second, the positivity of the loop correction $\langle \mu \rangle_L$, which increases the dipole moments of inclusions, directly accounts for the additional energy input into the polarization and the dipole–dipole interaction energies in the composites. Or, in other words, the positivity of $\langle \mu \rangle_L$ leads to a much higher energy storage in the composite. Our simulations show that the strength of $\langle \mu \rangle_L$ depends on the local arrangement of dipoles, such that the chained configurations host higher local fields. Therefore, the morphology of particle distribution, especially, an optimal assembly of chained configurations, is an essential factor in devising new composites with effective energy storage features.

It should be noted that our simulation model does not take into account the impurity ions in the polymer matrix and the free space charges in high-k fillers, which can greatly contribute to the pole formation on the filler surface, and also, perhaps, to the pole screening effects. The trapping of space charges at the inclusion pole sites can also form a remanent inclusion dipole moment when the external field is removed. We also ignore the existence of an interface between the inclusion and the matrix with an intermediate dielectric permittivity between ε_m and ε_p,[59,60] which, however, can be easily incorporated into our simulation model.

A Dielectric permittivity mixing rules for composite materials

Let us assume that a sphere of radius R containing N polarizable spherical particles of radius r and permittivity ε_p is

immersed in a medium with a permittivity ε_m. When the sphere is polarized under the applied field E, its dipole moment becomes

$$\vec{M} = 4\pi R^3 \varepsilon_0 \frac{\varepsilon_{eff} - \varepsilon_m}{\varepsilon_{eff} + 2\varepsilon_m} \vec{E} \qquad \text{(A.1)}$$

where ε_{eff} is the apparent permittivity of the sphere. It is straightforward to accept that

$$\vec{M} = N\vec{\mu}_p \qquad \text{(A.2)}$$

where $\vec{\mu}_p$ is the induced dipole moment of particles, for which we have

$$\vec{\mu}_p = 4\pi r^3 \varepsilon_0 \frac{\varepsilon_p - \varepsilon_m}{\varepsilon_p + 2\varepsilon_m} \vec{E}. \qquad \text{(A.3)}$$

Then, from eqn (A.1)–(A.3) we get

$$\frac{\varepsilon_{eff} - \varepsilon_m}{\varepsilon_{eff} + 2\varepsilon_m} = \eta \frac{\varepsilon_p - \varepsilon_m}{\varepsilon_p + 2\varepsilon_m} \qquad \text{(A.4)}$$

which is the Maxwell–Garnett (MG) equation, and the packing fraction of particles is defined as $\eta = Nr^3/R^3$. Eqn (A.4) can be solved to obtain ε_{eff} given by eqn (12) in the main text. The MG mixing rule is applicable for low η and does not take into account the interaction between induced dipoles $\vec{\mu}_p$.

Another approach to the mixing rule is based on considering both components, the inclusions and the host matrix, as perturbations to the local field in the composite. Each component is assumed to be formed from particles of spherical shape and embedded in a uniform effective media with ε_{eff}, which will be determined self-consistently. Considering that the average field in the composite is E, each inclusion will have an induced dipole

$$\vec{\mu}_p = 4\pi r^3 \varepsilon_0 \frac{\varepsilon_p - \varepsilon_{eff}}{\varepsilon_p + 2\varepsilon_{eff}} \vec{E} \qquad \text{(A.5)}$$

and, similarly, each matrix particle will develop a dipole moment

$$\vec{\mu}_m = 4\pi r^3 \varepsilon_0 \frac{\varepsilon_m - \varepsilon_{eff}}{\varepsilon_m + 2\varepsilon_{eff}} \vec{E}. \qquad \text{(A.6)}$$

Both these dipoles will change the local field E, and it is straightforward to assume that the contributions from these dipoles compensate each other in order to keep E unchanged. This condition can be written as

$$N_p \vec{\mu}_p + N_m \vec{\mu}_m = 0 \qquad \text{(A.7)}$$

where N_p and N_m are the number of inclusions and the matrix particles respectively. Then eqn (A.7) can be rewritten as

$$\eta \frac{\varepsilon_p - \varepsilon_{eff}}{\varepsilon_p + 2\varepsilon_{eff}} + (1 - \eta) \frac{\varepsilon_m - \varepsilon_{eff}}{\varepsilon_m + 2\varepsilon_{eff}} = 0. \qquad \text{(A.8)}$$

This is a quadratic Bruggeman (BR) equation for ε_{eff} and has two solutions. One of them is a physically sensible solution and is given by eqn (13) in the main text. The other solution is typically negative and has no physical meaning.

References

1 I. A. Anderson, T. A. Gisby, T. G. McKay, B. M. O'Brien and E. P. Calius, Multi-functional dielectric elastomer artificial muscles for soft and smart machines, *J. Appl. Phys.*, 2012, **112**, 041101.

2 F. Carpi, D. De Rossi, R. Kornbluh and R. E. Pelrine, *Dielectric elastomers as electromechanical transducers: fundamentals, materials, devices, models and applications of an emerging electroactive polymer technology*, Elsevier, Oxford, 2008.

3 S. Chiba, M. Waki, T. Wada, Y. Hirakawa, K. Masuda and T. Ikoma, Consistent ocean wave energy harvesting using electroactive polymer (dielectric elastomer) artificial muscle generators, *Appl. Energy*, 2013, **104**, 497–502.

4 O. Philippova, A. Barabanova, V. Molchanov and A. Khokhlov, Magnetic polymer beads: Recent trends and developments in synthetic design and applications, *Eur. Polym. J.*, 2011, **47**, 542–559.

5 C. A. Grabowski, H. Koerner, J. S. Meth, A. Dang, C. M. Hui, K. Matyjaszewski, M. Bockstaller, M. F. Durstock and R. A. Vaia, Performance of Dielectric Nanocomposites: Matrix-Free, Hairy Nanoparticle Assemblies and Amorphous Polymer-Nanoparticle Blends, *ACS Appl. Mater. Interfaces*, 2014, **6**, 21500–21509.

6 R. E. Newnham, Molecular mechanisms in smart materials, *Mater. Res. Bull.*, 1997, **22**, 20–34.

7 N. H. Chuc, J. C. Koo, Y. K. Lee, J. D. Nam and H. R. Choi, Artificial Muscle Actuator Based on the Synthetic Elastomer, *Int. J. Control Autom. Syst.*, 2008, **6**, 894–903.

8 L. S. McCarty and G. M. Whitesides, Electrostatic charging due to separation of ions at interfaces: contact electrification of ionic electrets, *Angew. Chem., Int. Ed.*, 2008, **47**, 2188–2207.

9 P. Brochu and Q. Pei, Advances in dielectric elastomers for actuators and artificial muscles, *Macromol. Rapid Commun.*, 2010, **31**, 10–36.

10 X. Zhang, G. Sessler and J. Hillenbrand, Improvement of piezoelectric coefficient of cellular polypropylene films by repeated expansions, *J. Electrost.*, 2007, **65**, 94–100.

11 J. Hillenbrand and G. M. Sessler, DC-based ferroelectrets with large piezoelectric d33 coefficients, *J. Appl. Phys.*, 2008, **103**, 074103.

12 J. D. Nam, H. R. Choi, J. C. Koo, Y. K. Lee and K. J. Kim, *Dielectric Elastomers for Artificial Muscles, Electroactive Polymers for Robotic Applications*, Springer, London, 2007, pp. 37–48.

19114 | *Phys. Chem. Chem. Phys.*, 2016, **18**, 19103–19117

This journal is © the Owner Societies 2016

13 D. L. Henann, S. A. Chester and K. Bertoldi, Modeling of dielectric elastomers: Design of actuators and energy harvesting devices, *J. Mech. Phys. Solids*, 2013, **61**, 2047–2066.

14 D. Ponnamma, K. K. Sadasivuni, Y. Grohens, Q. Guo and S. Thomas, Carbon nanotube based elastomer composites-an approach towards multifunctionl materials, *J. Mater. Chem. C*, 2014, **2**, 8446–8485.

15 A. O'Halloran, F. O'Malley and P. McHugh, A review on dielectric elastomer actuators, technology, applications and challenges, *J. Appl. Phys.*, 2008, **104**, 071101.

16 K. Zimmermann, V. A. Naletova, I. Zeidis, V. Böhm and E. Kolev, Modelling of locomotion systems using deformable magnetizable media, *J. Phys.: Condens. Matter*, 2006, **18**, S2973–S2983.

17 D. Szabo, G. Szeghy and M. Zrinyi, Shape transition of magnetic field sensitive polymer gels, *Macromolecules*, 1998, **1**, 6541–6548.

18 R. V. Ramanujan and L. L. Lao, The mechanical behavior of smart magnet-hydrogel composites, *Smart Mater. Struct.*, 2006, **15**, 952–956.

19 H. X. Deng, X. L. Gong and L. H. Wang, Development of an adaptive tuned vibration absorber with magnetorheological elastomer, *Smart Mater. Struct.*, 2006, **15**, N111–N116.

20 T. L. Sun, X. L. Gong, W. Q. Jiang, J. F. Li, Z. B. Xu and W. H. Li, Study on the damping properties of magnetorheological elastomers based on *cis*-polybutadiene rubber, *Polym. Test.*, 2008, **27**, 520–526.

21 Z. Suo, Theory of dielectric elastomers, *Acta Mech. Solida Sin.*, 2010, **23**, 549–578.

22 P. Bawa, V. Pillay, Y. E. Choonara and L. C du Toit, Stimuli-responsive polymers and their applications in drug delivery, *Biomed. Mater.*, 2009, **4**, 022001.

23 H. Xu, C. Wang, C. Wang, J. Zoval and M. Madou, Polymer actuator valves toward controlled drug delivery application, *Biosens. Bioelectron.*, 2006, **21**, 2094–2099.

24 L. C. Branquinho, M. S. Carria, A. S. Costa, N. Zufelato, M. H. Sousa, R. Miotto, R. Ivkov and A. F. Bakuzis, Effect of magnetic dipolar interactions on nanoparticle heating efficiency: Implications for cancer hyperthermia, *Sci. Rep.*, 2013, **3**, 2887.

25 S. Zabel, C. Kirchhof, E. Yarar, D. Meyners, E. Quandt and F. Faupel, Phase modulated magnetoelectric delta-E effect sensor for sub-nano tesla magnetic fields, *Appl. Phys. Lett.*, 2015, **107**, 152402.

26 S. Chiba and M. Waki, in *Extending applications of dielectric elastomer artificial muscles to wireless communication systems*, ed. J. C. Lin, Recent advances in Wireless Communications and Networks, 2011, pp. 435–454, ISBN 978-953-307-274-6.

27 T. Mirfakhrai, J. D. W. Madden and R. H. Baughman, Polymer Artificial Muscles, *Mater. Today*, 2007, **10**, 30–38.

28 K. S. Ramadan, D. Sameoto and S. Evoy, A review of piezo-electric polymers as functional materials for electromechanical transducers, *Smart Mater. Struct.*, 2014, **23**, 033001.

29 E. Allahyarov, L. Zhu and H. Löwen, Analysis of the actuation properties of charged multilayer films, *J. Appl. Phys.*, 2015, **117**, 034504.

30 E. Allahyarov, A. M. Menzel, L. Zhu and H. Löwen, Magneto-mechanical response of bilayered magnetic elastomers, *Smart Mater. Struct.*, 2014, **23**, 115004.

31 Q. Xunlin, X. Zhongfu and W. Feipeng, Piezoelectricity of single- and multi-layer cellular polypropylene film electrets, *Front. Mater. Sci. China*, 2007, **1**, 72–75.

32 C. R. Bowen and V. Yu. Topolov, Piezoelectric sensitivity of PbTiOs based ceramic/polymer composites with.0-3 and 3-3 connectivity, *Acta Mater.*, 2003, **51**, 4964–4976.

33 D. A. van den Ende, B. F. Bory, W. A. Groen and A. van der Zwaag, Improving the d33 and g33 properties of 0-3 piezo-electric composites by dielectrophoresis, *J. Appl. Phys.*, 2010, **107**, 024107.

34 B. Pawlik, C. Schirrmann, K. Bornhorst and F. Costache, Strain-enhanced Nanocomposites of Electrostrictive Polymers and High-k Nanofillers for Micro-actuation Applications, *Procedia Eng.*, 2014, **87**, 1601–1604.

35 F. Faupel, V. Zaporojtchenko, T. Strunskus and M. Elbahri, Metal-Polymer Nanocomposites for Functional Applications, *Adv. Eng. Mater.*, 2010, **12**, 1177–1190.

36 R. Shankar, T. K. Ghosh and R. J. Spontak, Mechanical and actuation behavior of electroactive nanostructured polymers, *Sens. Actuators, A*, 2009, **151**, 46–52.

37 P. H. Vargantwar, R. Shankar, A. S. Krishnan, T. K. Ghosh and R. Spontak, Exceptional versatility of solvated block copolymer/ionomer networks as electroactive polymers, *Soft Matter*, 2011, **7**, 1651–1655.

38 R. Pelrine, R. Kornbluh, J. Joseph, R. Heydt, Q. Pei and S. Chiba, High-field electrostriction of elastomeric dielectrics for actuators, *Mater. Sci. Eng., C: Biomimetic Mater., Sens. Syst.*, 2000, **11**, 89–100.

39 Y. Han, W. Hong and L. E. Faidley, Field-stiffening effect of magneto-rheological elastomers, *Int. J. Solids Struct.*, 2013, **50**, 2281–2288.

40 A. Singh, M. Shirolkar, M. V. Limaye, S. Gokhale, C. Khan-Malek. and S. K. Kulkarni, A magnetic nano-composite soft polymeric membrane, *Microsyst. Technol.*, 2013, **19**, 409–418.

41 B. A. Evans, B. L. Fiser, W. J. Prins, D. J. Rapp, A. R. Shields, D. R. Glass and R. Superfine, A highly tunable silicone-based magnetic elastomer with nanoscale homogeneity, *J. Magn. Magn. Mater.*, 2012, **324**, 501–507.

42 B. Sareni, L. Krahenbuhl, A. Beroual and C. Brosseau, Effective dielectric constant of periodic composite materials, *J. Appl. Phys.*, 1996, **80**, 1688–1696.

43 T. C. Choy, *Effective Medium Theory*, Clarendon Press, Oxford, 1999, ISBN 978-0-19-851892-1.

44 Y. WU, X. Zhao, F. Li and Z. Fan, Evaluation of mixing rules for dielectric constants of composite dielectrics by MC-FEM calculation on 3D cubic lattice, *J. Electroceram.*, 2003, **11**, 227–239.

45 F. Deng and K. Van Vliet, Prediction of elastic properties for polymer-particle nanocomposites exhibiting an interphase, *Nanotechnology*, 2011, **22**, 165703.

46 S. Y. Fu, X. Q. Feng, B. Lauke and Y. W. Mai, Effects of particle size, particle/matrix interface adhesion and particle

loading on mechanical properties of particulate-polymer composites, *Composites, Part B*, 2008, **39**, 933–961.

47 A. Upadhyay and R. Singh, Prediction of effective elastic modulus of biphasic composite materials, *Mod. Mech. Eng.*, 2012, **2**, 6–13.

48 D. Ivaneyko, V. Toshchevikov, M. Saphiannikova and G. Heinrich, Magneto-sensitive elastomers in a homogeneous magnetic field: a regular rectangular lattice model, *Macromol. Theory Simul.*, 2011, **20**, 411–424.

49 D. Ivaneyko, V. Toshchevikov, M. Saphiannikova and G. Heinrich, Effects of particle distribution on mechanical properties of magneto-sensitive elastomers in a homogeneous magnetic field, *Condens. Matter Phys.*, 2012, **15**, 33601.

50 D. Ivaneyko, V. Toshchevikov, M. Saphiannikova and G. Heinrich, Mechanical properties of magneto-sensitive elastomers: unification of the continuum-mechanics and microscopic theoretical approaches, *Soft Matter*, 2014, **10**, 2213–2225.

51 A. Yu. Zubarev, Magneto-deformation of ferrogels and ferro-elastomers. Effect of microstructure of the particles spatial disposition, *Physica A*, 2013, **392**, 4824–4836.

52 A. Yu. Zubarev and A. S. Elkady, Magnetodeformation and elastic properties of ferrogels and ferroelastomers, *Physica A*, 2014, **413**, 400–408.

53 K. Morozov, M. Shliomis and H. Yamaguchi, Magnetic deformation of ferrogel bodies: Procrustes effect, *Phys. Rev. E: Stat., Nonlinear, Soft Matter Phys.*, 2009, **79**, 040801.

54 E. Allahyarov, H. Löwen and L. Zhu, A simulation study of the electrostriction effects in dielectric elastomer composites containing polarizable inclusions with different spatial distributions, *Phys. Chem. Chem. Phys.*, 2015, **17**, 32479–32497.

55 G. Zhang, D. Dong, D. Brannum, L. Tang, E. Allahyarov, S. Tang, J.-K. Lee and L. Zhu, Interfacial Polarization-Induced Loss Mechanisms in Polypropylene/BaTiO₃ Nano-composite Dielectrics, *Chem. Mater.*, 2016, DOI: 10.1021/acs.chemmater.6b01383.

56 Q. Wang and L. Zhu, Polymer Nanocomposites for Electrical Energy Storage, *J. Polym. Sci., Part B: Polym. Phys.*, 2011, **49**, 1421–1429.

57 Z.-M. Dang, J.-K. Yuan, S.-H. Yao and R.-J. Liao, Flexible nanodielectric materials with high permittivity for power energy storage, *Adv. Mater.*, 2013, **25**, 6334–6365.

58 L. A. Fredin, Z. Li, M. T. Lanagan, M. A. Ratner and T. J. Marks, Substantial Recoverable Energy Storage in Percolative Metallic Aluminum-Polypropylene Nanocomposites, *Adv. Funct. Mater.*, 2013, **23**, 3560–3569.

59 H. T. Vo and F. G. Shi, Towards model-based engineering of optoelectronic packaging materials: dielectric constant modeling, *Microelectron. J.*, 2002, **33**, 409–415.

60 J. Y. Li, L. Zhang and S. Ducharme, Electric energy density of dielectric nanocomposites, *Appl. Phys. Lett.*, 2007, **90**, 132901.

61 W. Li, Q. Meng, Y. Zheng, Z. Zhang and W. Xia, Zhuo Xu Electric energy storage properties of poly(vinylidene fluoride), *Appl. Phys. Lett.*, 2010, **96**, 192905.

62 V. Ranjan, M. B. Nardelli and J. Bernholc, Electric Field Induced Phase Transitions in Polymers: A Novel Mechanism for High Speed Energy Storage, *Phys. Rev. Lett.*, 2012, **108**, 087802.

63 R. Han, J. Jin, P. Khanchaitit, J. Wang and Q. Wang, Effect of crystal structure on polarization reversal and energy storage of ferroelectric poly(vinylidene fluoride-co-chlorotrifluoro-ethylene) thin films, *Polymer*, 2012, **53**, 1277–1281.

64 Q. Wang and L. Zhu, Polymer Nanocomposites for Electrical Energy Storage, *J. Polym. Sci., Part B: Polym. Phys.*, 2011, **49**, 1421–1429.

65 F. Guan, J. Wang, J. Pan, Q. Wang and L. Zhu, Effects of Polymorphism and Crystallite Size on Dipole Reorientation in Poly(vinylidene fluoride) and Its Random Copolymers, *Macromolecules*, 2010, **43**, 6739–6748.

66 F. Guan, J. Pan, J. Wang, Q. Wang and L. Zhu, Crystal Orientation Effect on Electric Energy Storage in Poly-(vinylidene fluoride-co-hexafluoropropylene) Copolymers, *Macromolecules*, 2010, **43**, 384–392.

67 O. Levy and D. Stroud, Maxwell Garnett theory for mixtures of anisotropic inclusions: Application to conducting polymers, *Phys. Rev. B: Condens. Matter Mater. Phys.*, 1997, **56**, 8035–8046.

68 E. Tuncer, Dielectric mixtures: importance and theoretical approaches, *IEEE Electr. Insul. Mag.*, 2013, **29**, 49–58.

69 E. Tuncer, S. M. Gubanski and B. Nettelblad, Dielectric relaxation in dielectric mixtures: application of the nite element method and its comparison with mixture formulas, *J. Appl. Phys.*, 2001, **89**, 8092–8100.

70 L. Gao and J. Z. Gu, Effective dielectric constant of a two-component material with shape distribution, *J. Phys. D: Appl. Phys.*, 2001, **35**, 267–271.

71 D. A. G. Bruggeman, Berechnung verschiedener physikalischer konstanten von heterogenen substanzen, i. dielektrizitätskon-stanten und leitfähigkeiten der mischkörper aus isotropen substanzen, *Ann. Phys.*, 1935, **24**, 636–664.

72 P. N. Sen, C. Scala and M. H. Cohen, A self-similar model for sedimentary rocks with application to the dielectric constant of fused glass beads, *Geophysics*, 1981, **46**, 781–795.

73 R. Skomski, J. Li, J. Zhou and D. J. Sellmyer, Multiscale Phenomena in Bruggeman Composites, *Mater. Res. Soc. Symp. Proc.*, 2005, **851**, 1.7.1–1.7.12.

74 R. Skomski, B. Balamurugan, E. Schubert, A. Enders and D. J. Sellmyer, Length scales of interactions in magnetic, dielectric and mechanical nanocomposites, *Mater. Res. Soc. Symp. Proc.*, 2011, **1312**, 171–182.

75 O. Levy and D. Stroud, Maxwell Garnett theory for mixtures of anisotropic inclusions: Application to conducting polymers, *Phys. Rev. B: Solid State*, 1997, **56**, 8035–8046.

76 A. Sihvola, *Electromagnetic Mixing Formulas and Applications*, IEE Publishing, London, 1990.

77 P. P. Bansal and A. J. Ardell, Average nearest-neighbor distances between uniformly distributed finite particles, *Metallography*, 1972, **5**, 97–111.

78 M. P. Allen and D. J. Tildesley, *Computer Simulation of Liquids*, Clarendon press, Oxford, 1989.

79 Z. Wang, C. Holm. Estimate of the cutoff errors in the Ewald summation for dipolar systems, *J. Chem. Phys.*, 2001, **115**, 6351–6359.

80 A. P. Hynninen and M. Dijkstra, Phase behavior of dipolar hard and soft spheres, *Phys. Rev.*, 2005, **72**, 051402.

81 C. Spieler, M. Kästner, J. Goldmann, J. Brummund and V. Ulbricht, XFEM modeling and homogenization of magneto-active composites, *Acta Mech.*, 2013, **224**, 2453–2469.

82 N. Chawla, R. S. Sidhu and V. V. Ganesh, Three-dimensional visualization and microstructure-based modeling of deformation in particle-reinforced composites, *Acta Mater.*, 2006, **54**, 1541–1548.

83 L. An, S. A. Boggs and J. P. Callame, Energy storage in polymer films with high dielectric constant fillers, *IEEE Electr. Insul. Mag.*, 2008, **24**, 5–10.

84 K. K. Kärkkäinen, A. H. Sihvola and K. I. Nikoskinen, Effective Permittivity of Mixtures: Numerical Validation by the FDTD Method, *IEEE Trans. Geosci. Remote Sens.*, 2000, **38**, 1303–1308.

85 S. K. Patil, M. Y. Koledintseva, R. W. Schwartz and W. Huebner, Prediction of effective permittivity of diphasic dielectrics using an equivalent capacitance model, *J. Appl. Phys.*, 2008, **104**, 074108.

86 A. Sihvola and I. Lindell, Polarizability modeling of heterogeneous media, in *Dielectric Properties of Heterogeneous Materials*, ed. A. Priou, PIER 6 Progress in Electromagnetics Research, Elsevier, Amsterdam, The Netherlands, 1992, pp. 101–151.

87 T. E. Doyle, D. A. Robinson, S. B. Jones, K. H. Warnick and B. L. Carruth, Modeling the permittivity of two-phase media containing monodisperse spheres: effects of microstructure and multiple scattering, *Phys. Rev. B: Solid State*, 2007, **76**, 054203.

88 H. Cheng and S. Torquato, Electric-field fluctuations in random dielectric composites, *Phys. Rev. B: Solid State*, 1997, **56**, 8060–8068.

89 S. A. Paniagua, Y. Kim, K. Henry, R. Kumar, J. W. Perry and S. R. Marder, Surface-initiated polymerization from Barium titanate nanoparticles for hybrid dielectric capacitors, *ACS Appl. Mater. Interfaces*, 2014, **6**, 3477–3482.

90 D. Gatti, H. Haus, M. Matysek, B. Frohnapfel, C. Tropea and H. F. Schlaak, The dielectric breakdown limit of silicone dielectric elastomer actuators, *Appl. Phys. Lett.*, 2014, **104**, 052905.

This journal is © the Owner Societies 2016

Phys. Chem. Chem. Phys., 2016, **18**, 19103–19117 | **19117**